ACS NANO

www.acsnano.org

ARTICLE

Bioresorbable Microdroplet Lasers as Injectable Systems for Transient Thermal Sensing and Modulation

Daniel Franklin, Tyler Ueltschi, Andrea Carlini, Shenglian Yao, Jonathan Reeder, Benjamin Richards, Richard P. Van Duyne, and John A. Rogers*

Cite This: *ACS Nano* 2021, 15, 2327−2339

Read Online

ACCESS | Metrics & More | Article Recommendations | Supporting Information

ABSTRACT: **Minimally invasive methods for temperature sensing and thermal modulation in living tissues have extensive applications in biological research and clinical care. As alternatives to bioelectronic devices for this purpose, functional nanomaterials that self-assemble into optically active microstructures offer important features in remote sensing, injectability, and compact size. This paper introduces a transient, or bioresorbable, system based on injectable slurries of well-defined microparticles that serve as photopumped lasers with temperature-sensitive emission wavelengths (>4−300 nm °C^{-1}). The resulting platforms can act as tissue-embedded thermal sensors and, simultaneously, as distributed vehicles for thermal modulation. Each particle consists of a spherical resonator formed by self-organized cholesteric liquid crystal molecules doped with fluorophores as gain media, encapsulated in thin shells of soft hydrogels that offer adjustable rates of bioresorption through chemical modification. Detailed studies highlight fundamental aspects of these systems including particle sensitivity, lasing threshold, and size. Additional experiments explore functionality as photothermal agents with active temperature feedback (ΔT = 1 °C) and potential routes in remote evaluation of thermal transport properties. Cytotoxicity evaluations support their biocompatibility, and *ex vivo* demonstrations in Casper fish illustrate their ability to measure temperature within biological tissues with resolution of 0.01 °C. This collective set of results demonstrates a range of multifunctional capabilities in thermal sensing and modulation.**

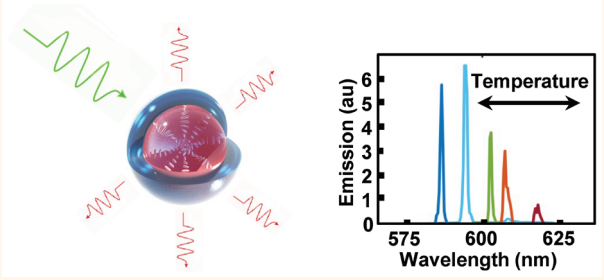

KEYWORDS: *temperature, self-organization, biodegradable, sensors, imaging*

The temperature of biological systems and its active regulation are essential for life processes in all advanced organisms. From metabolic and ionic activity at the cellular level to fluidic perfusion and immunological activity at the macro/organ-level, temperature affects tissue function, and deviations can indicate underlying illness and inform diagnosis. Once detected, active control of temperature can then serve as the basis for therapies to regulate chemical imbalances,[1] induce regional apoptosis,[2,3] or activate/disrupt neurological pathways.[4−6] Bioelectronic devices can provide many of these required functions, but they involve invasive methods for insertion and require electrical readout with associated interconnected traces, digital electronics, and/or antenna structures that have dimensions in the millimeter to centimeter range.[7,8] Functional nano/microparticle probes formed in biocompatible and bioresorbable materials and configured for injection, optical imaging, and remote sensing represent promising alternatives.[9,10] Additionally, fabrication of such systems from bioresorbable materials can lead to diagnostic and/or therapeutic functionality with a limited residence time in the body, engineered to coincide with a transient biological process such as wound healing.[11]

Recent strategies in remote temperature sensing exploit optically active materials, such as molecular probes,[12,13] upconversion nanoparticles,[14] or quantum dots[15,16] assembled into nano/microparticles[17−19] for direct injection into biological tissues. Careful selection of materials and structures enables excitation at wavelengths of relative tissue transparency, with consequent radiation of light that can pass back through the tissue for remote detection. Fluorescence imaging

Received: December 7, 2020
Accepted: January 5, 2021
Published: January 13, 2021

https://dx.doi.org/10.1021/acsnano.0c10234
ACS Nano 2021, 15, 2327−2339

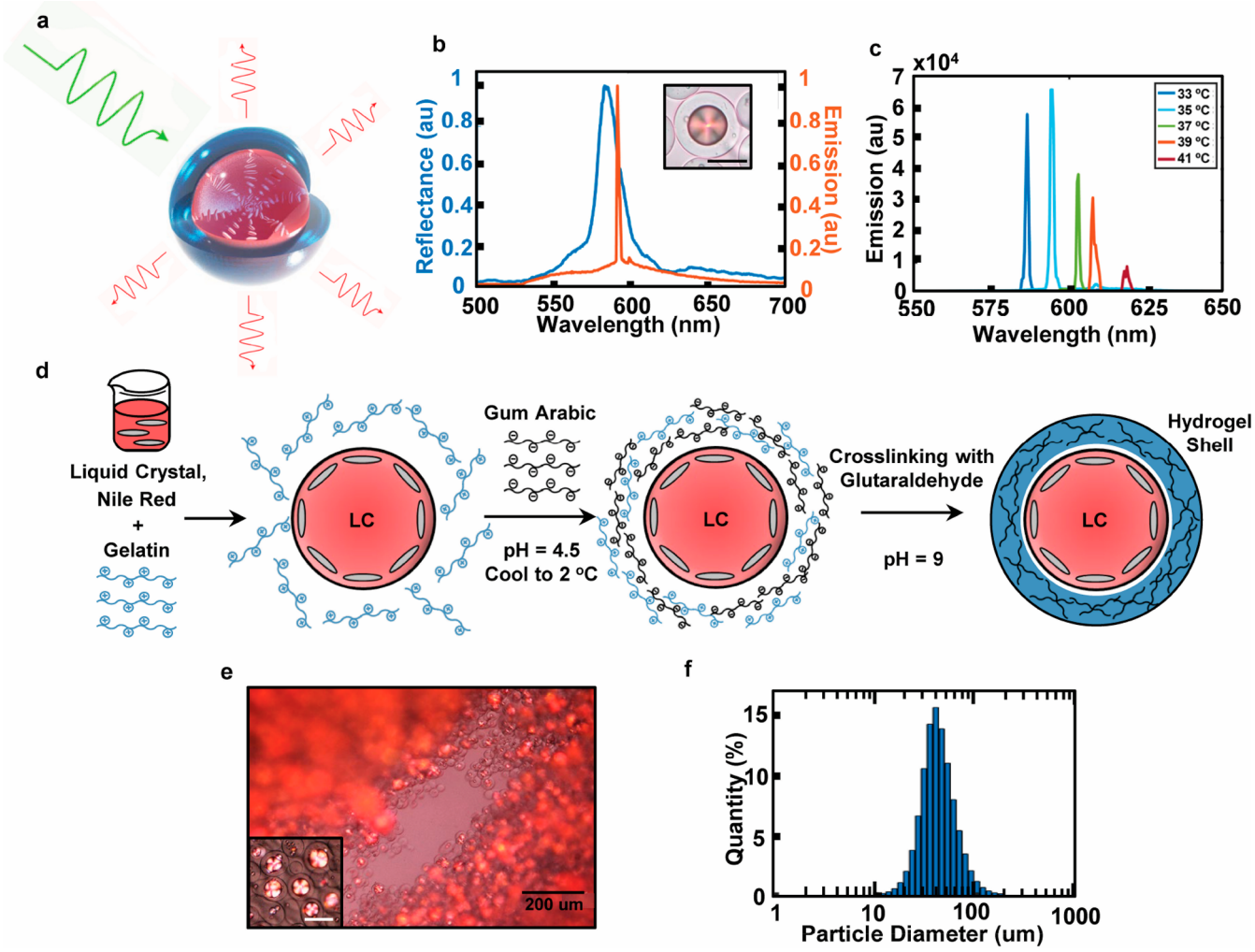

Figure 1. Bioresorbable microdroplet lasers for biological temperature sensors *via* complex coacervation. (a) Illustration of a gelatin encapsulated, dye-doped LC microdroplet laser with internal radial helix director profile. (b) Bragg reflectance due to the molecular helix and corresponding band-edge lasing when pumped with a nanosecond laser at 532 nm. Inset micrograph is of a single particle under crossed polarized illumination. Scale bar is 50 μm. (c) Temperature tunable lasing *via* changes in LC molecular helical pitch. (d) Schematic illustration of the complex coacervation fabrication process utilized to encapsulate LC droplets in shells of gelatin. (e) Micrographs depicting encapsulated particles "en masse" and the large-scale nature of complex coacervation production. Scale bar is 200 μm and inset scale bar is 50 μm. (f) Resulting particle distributions of LC microdroplets measured *via* laser scattering.

of this type allows for measurements of temperature in deep tissue *via* ratio-metric,[20,21] wavelength-shifting,[22] and time-resolved fluorescence[23] in which the amplitude, wavelength, or lifetime of fluorescence, respectively, correlate to local temperature. However, the wavelength-dependent absorption and scattering of biological tissue necessitates excitation power and depth calibration curves that are impractical for *in vivo* sensing where the exact optical path is uncertain.[24]

In contrast, methods that encode temperature to emission wavelength are undistorted by depth or optical path. Within this category of wavelength-tunable probes, micro/nanoparticle systems that support lasing provide attractive features such as narrow wavelength operation, high output intensity, and tunability through resonant cavity design.[10,17,25,26] These properties support enhanced sensitivity and create prospects for functionality in deep tissue locations through engineering of emission characteristics. Photonic crystal lasers that exploit dye-doped liquid crystals (LCs) offer the highest temperature sensitivity within this class of optical schemes.[27] However, these systems have largely been demonstrated with non-biologically compatible materials that persist within tissues and/or are toxic. In addition, such lasers have not been explored for localized thermal modulation.

This paper introduces a cholesteric liquid crystal (CLC) microdroplet laser composed of and encapsulated in biocompatible materials, including those designed to undergo complete bioresorption over controlled time scales. Here, biologically derived cholesteryl-esters and an organic fluorescent dye form the basis of tunable photopumped lasers *via* self-assembly into temperature-sensitive photonic cavities. When pumped optically, the particles emit laser light, with wavelengths that depend on the local temperature. Encapsulation in gelatin hydrogel shells *via* complex coacervation enables the large-scale production of sensors of this type, in forms that can be injected with a syringe into tissue locations of interest. Systematic evaluations of lasing dynamics define the underlying physics of operation and the functional bounds of this system in terms of key parameters such as sensitivity and minimum probe size. Quantitative measurements of laser-induced heating lead to three independent modes of operation:

https://dx.doi.org/10.1021/acsnano.0c10234
ACS Nano 2021, 15, 2327−2339

(1) temperature sensing, where self-heating is minimal, (2) thermal modulation, where temperature sensing accompanies laser-induced heating to establish a closed-feedback loop for active control, and (3) rapid and minute modulation of probe temperature, where analysis of decay profiles yields thermal transport properties of the surounding media. Accelerated enzymatic degradation studies reveal the chemical mechanisms of bioresorption of the hydrogel shell with kinetics that can be tuned through shell cross-linking. Cytotoxicity assays using mouse L929 cells demonstrate basic biocompatibility of the materals and the products of their degradation. Injection and characterization of lasing within Casper fish models, *ex vivo*, highlights the functionality of the microdroplets in biological tissues. Taken together, the results presented here demonstrate multifunctional capabilities in both active and passive thermal interfaces to living systems, with possibilities for immediate use in biological research and with the potential for future application in diagnostic and therapeutic clinical procedures.

RESULTS AND DISCUSSION

Dye-Doped Liquid Crystal Droplet Laser. Figure 1a illustrates the structure and function of the microdroplet laser, the core of which consists of a cholesteryl ester compound (47 wt % cholesteryl oleyl carbonate (COC), 26 wt % cholesteryl nonanoate (CN), 26 wt % cholesteryl chloride (CC)), and a uniformly dispersed organic fluorescent dye (1 wt % nile red). The CLC exhibits a radial-helical molecular director when confined to a spherical geometry and creates periodic variations in refractive index radially throughout the droplet.[28,29] This variation leads to a photonic band gap/Bragg reflection for circularly polarized light with the same handedness at a wavelength determined by the helical pitch. Overlap of this bandgap with the emission profile of the fluorescent dye yields a resonant laser cavity in which amplified spontaneous and stimulated emission can occur when optically pumped with a pulsed laser at a wavelength that overlaps with the absorption of the dye,[30] in this case a frequency doubled, Q-switched Nd:YAG laser at 532 nm. Figure 1b shows the reflectance due to the photonic band gap as well as the lasing peak that manifests at the band edge when optically excited above the lasing threshold. Each particle is an independent lasing cavity and functioning sensor. The micrograph inset depicts a representative particle when viewed through cross-polarizers. The dark cross results from the radial-helical orientation of the LC molecules.[31]

The pitch of the molecular helix is sensitive to temperature through changes in intermolecular distance and order. The composition of the LC compound[32] defines the functional wavelength and temperature range (known within the LC industry as "color play"). The temperature dependence of this system translates to the resonant wavelength of the cavity, resulting in a temperature-sensitive microdroplet laser in which wavelength can be tuned throughout the emission band of the fluorescent dye. Figure 1c shows the laser emission of a representative CLC microdroplet (47 wt % COC, 26 wt % CN, 26 wt % CC) as a function of temperature with a corresponding sensitivity of ~4 nm $^{\circ}C^{-1}$. Increased sensitivities can be achieved with LCs that exhibit phase transitions near the range of operating temperatures.[32] As an example, Supplementary Figure S1 shows the reflection spectrum (as measured within a parallel-plate LC cell) of the compound above and a compound (30 wt % COC, 60 wt % CN, 10 wt % cholesteryl dichlorobenzene (CD)) that exhibits a nonlinear temperature response, with a peak sensitivity in excess of −300 nm $^{\circ}C^{-1}$. This large, negative sensitivity originates from a phase transition from cholesteric to smectic A, in which the chiral molecular orientation rapidly "unwinds" to yield a stratified and layered vertical orientation. The tunable and exceptionally high sensitivities that are possible in these systems represent significant advantages over alternative materials and modalities for temperature sensing. Supplementary Figure S1 also compares the shift in Bragg reflectance based on confinement for the CLC compound within a parallel-plate cell and a microsphere, respectively.

Encapsulating the CLC microdroplets in shells formed with a cross-linked hydrogel (50% porcine skin gelatin, 50% gum acacia; thicknesses up to 30 μm) *via* complex coacervation[33] stabilizes and protects the cholesteric core from surrounding biological environments. This process is amenable to large-scale microencapsulation,[34] as demonstrated by its commercial use in the food/cosmetics industries and for certain thermochromic LC products.[35] As illustrated in Figure 1d, the process begins with an emulsion of the dye-doped CLC compound in 10 wt % gelatin in DI water under constant agitation. Adding a solution of 10 wt % gum acacia and slowly lowering the pH to 4.5 causes the gelatin/gum acacia copolymers to aggregate and nucleate on adjacent interfaces, including those associated with the CLC microdroplets. The phase separation is mediated by electrostatic interactions among the charged macromolecules, and the resulting thickness of the hydrogel can be controlled through the pH and initial concentrations of the copolymers. Supplementary Figure S2 illustrates the uniformity of the shell thicknesses for microdroplets with a range of sizes and demonstrates independent control of this thickness *via* the solution pH. The integrity of the shells relies on weak ionic attractions due to the opposite charges of the gelatin and gum acacia polymers. Cooling the mixture to 2 °C and increasing the pH to 9 promote solidification. Addition of a cross-linker (0−5 wt % glutaraldehyde) to covalently bond the gelatin and gum acacia polymers yields a shell that is mechanically robust in biological environments.[36] Iterative centrifuging and rinsing of the microparticle slurry with phosphate buffered saline (PBS) solution eliminates any excess cross-linker from the solution and porous hydrogel.

The surface energy and alignment imposed at the core−shell interface represents a key consideration for the encapsulant material. As signified by the gray ellipsoids within the schematic illustration of Figure 1d, an interfacial planar (homogeneous) alignment is essential for the proper radial-helical alignment throughout the LC core and therefore to the function and tunability of the droplet laser. While some encapsulants impart vertical (homeotropic) alignment and require additional planar alignment layers,[29] the gelatin hydrogel reported here supports the desired planar orientation, consistent with literature[37] and the cross-polarized microscopy results of Figure 1b. Storage and use of the encapsulated particles in PBS further ensure the desired core alignment within aqueous environments at ion concentrations similar to those encountered *in vivo*.

The sizes and shapes of the CLC microdroplets depend strongly on parameters such as the agitation method/speed, solution viscosity/particle density, and rate of pH changes. Careful control of these conditions can yield large quantities of particles with spherical shapes and narrow size distributions, as in Figure 1e. Measurements with a laser diffraction size

https://dx.doi.org/10.1021/acsnano.0c10234
ACS Nano 2021, 15, 2327−2339

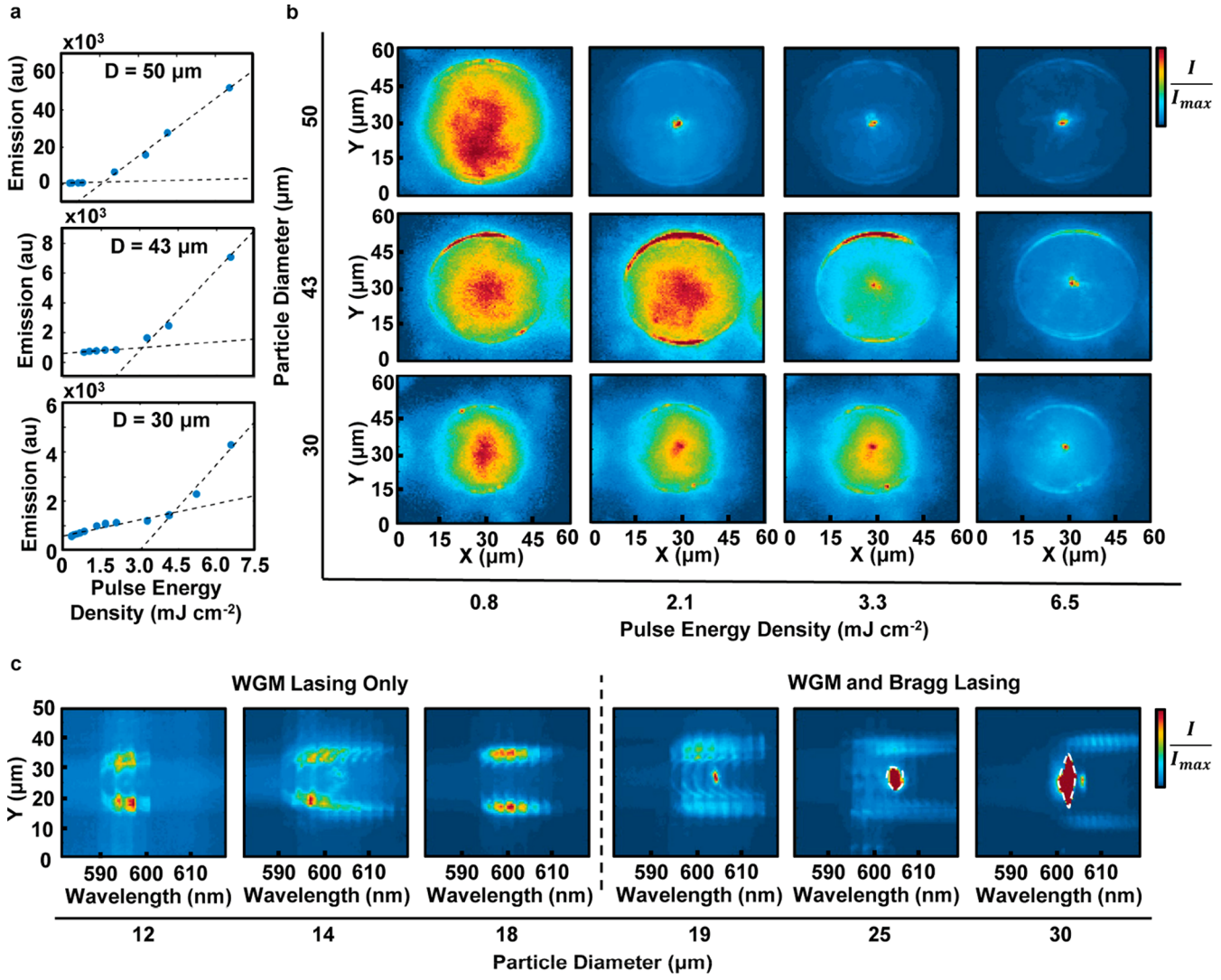

Figure 2. Single-particle lasing characteristics. (a) Emission from single particles of varying diameters as a function of excitation energy. The intersection of the two emission slopes represents the lasing threshold which is inversely related to particle size. (b) Imaging spectrographs of the particles in (a). Particle-wide spontaneous emission collapses to a point of stimulated emission emanating from center of the LC droplet resonator and in all directions. (c) Imaging spectrographs of particles as a function of diameter illustrating the smallest particles to exhibit Bragg lasing of 19 μm at an incident energy of 7.5 mJ cm^{-2}. Whispering gallery mode emission is present on the surfaces of all droplets but is largely overtaken by Bragg lasing as particles increase in size.

analyzer reveal a log-normal size distribution centered at a diameter of 30 μm for the CLC cores, as in Figure 1f. As an aside, oblong cores and/or asymmetric shells can also be obtained through flow-induced effects, without altering the molecular orientation of the inner core. Supplementary Figure S3 shows optical micrographs of various such asymmetric particles under cross-polarized reflected light. The dark cross patterns in these images are consistent with radial-helical molecular orientations. The central reflectance points indicate the effective formation of photonic band gap/Bragg resonances and consequent lasing upon excitation. These results suggest robustness in the Bragg lasing phenomena within the particles and an associated leniency in fabrication requirements and relative invariance to external forces and geometrical distortions.[29]

Lasing Dynamics. Optically pumping the CLC microdroplets with nanosecond pulses of light (wavelength: 532 nm; repetition rate: 10 Hz; spot size: 65 μm diameter, Supplementary Figure S4; energy: up to 1 μJ) from a frequency-doubled Q-switched neodymium-doped yttrium-aluminum-garnet (Nd:YAG) laser elucidates the lasing mechanisms. An imaging spectrograph resolves the resulting emission after a long pass filter that removes pump laser light. The lasing threshold depends on particle size, as depicted in Figure 2a for particles with diameters of 30, 43, and 50 μm. At pumping energies below the lasing threshold, spontaneous emission occurs with an efficiency defined by the nile red fluorescent dye.[38,39] As the excitation energy increases, the rate of change in the emission intensity with the energy increases significantly and abruptly. The emission curve highlights these two regimes (lasing and nonlasing), and the intersection corresponds to the lasing threshold. Figure 2b shows spectrograph images of the corresponding particles for selected energies. When shown spatially, the differences between nonlasing and lasing states are even more apparent. Below lasing, spontaneous emission occurs throughout the entire particle, the intensity of which is proportional to the projection of the fluorescent dye density on the image plane. At the onset

https://dx.doi.org/10.1021/acsnano.0c10234
ACS Nano 2021, 15, 2327−2339

of lasing, the emission intensity becomes highly localized to the center of the particle, indicative of the radial resonant mode within the photonic cavity.

The dependence of lasing threshold on particle size can be attributed to changes in the resonant strength of the CLC cavity and the amount of nonquenched dye available for stimulated emission.[40,41] Analytical forms for lasing threshold originate from the laser rate equations[42] and/or density of state considerations,[41] but result in the following dependence on particle diameter:[40] $E_{th} = Ad + B/d^2$, where E_{th} is lasing threshold, d is particle diameter, and A and B are constants. Increasing the particle size increases the number of periods of the molecular helix within the droplet, thereby enhancing coherent scattering and increasing both the amplitude of the Bragg reflectance and the efficiency of the resonant cavity, Q. Conversely, decreasing the particle size reduces the resonance efficiency of the radial cavity and decreases the amount of excitable gain medium through the smaller volume of the particle. This trend suggests that there is a minimum particle diameter below which lasing cannot occur. To explore this behavior, Figure 2c presents a series of spectrograph images for particles with a range of diameters, each optically pumped at an energy density of 7.5 mJ cm^{-2}. Here, the spectral composition of the emission is shown instead of the spatial x-axis. At diameters below 19 μm, whispering gallery mode (WGM) lasing occurs at the edge of the microdroplets due to the difference in refractive index of the LC and that of the surrounding medium. For diameters of 19 μm and above, a lasing peak forms at the center of the particle (in addition to WGM lasing) and is consistent with lasing from the radial Bragg resonance. While WGM lasing can exhibit some sensitivity to temperature due to thermally induced changes in refractive index ((0.08 nm °C^{-1}),[14] (0.96 nm °C^{-1})[43]), lasing from CLC Bragg reflectance is 2−3 orders of magnitude more sensitive and can be tuned/engineered for specific temperature and wavelength ranges. Also, the peak emission wavelengths of WGM lasing depend strongly on particle size,[43] which will translate fabrication errors/distributions to subsequent temperature measurements. In contrast, Bragg resonance lasing depends only on molecular pitch of the CLC compound. For these reasons, Bragg lasing is highly preferable for temperature sensing.

This minimum diameter for Bragg lasing depends on the efficiency/concentration of the fluorescent dye,[44] the resonant cavity efficiency (Q), the pump energy, and additional factors.[40] Supplementary Figure S5 demonstrates lasing characteristics of microdroplets as a function of nile red concentration. Results show that an optimized dye concentration between 1% and 1.5% leads to the lowest lasing threshold and highest lasing efficiency. Loading above 2% leads to particulate formation and significant quenching. Supplementary Figure S6 analyzes the full-width-half-max (fwhm) and resonance efficiencies of Bragg reflectance (fwhm = 24 nm), lasing emission at threshold (fwhm = 1.75 nm), and highly driven lasing (fwhm = 0.1 nm) for a 50 μm particle. The Q-factor of the lasing system is approximated by $Q = \frac{\lambda_0}{\text{fwhm}}$ at the lasing threshold, which results in a Q-factor of 341. LC materials with higher birefringence could increase this resonance efficiency and thereby reduce this minimum diameter, with limits in the range of 10 μm originating from a minimum number of helical periods to effectively reflect light.[40] Decreasing the pump pulse length represents another strategy for decreasing the lasing threshold and the minimum functional particle size.

Laser-Induced Heating and Additional Modalities. The significance of laser-induced heating can be determined by tracking the Bragg lasing wavelength of a particle after subsequent excitation pulses. For a spherical particle of arbitrary material, the time for heat to conduct to the surrounding medium is characterized by $\tau_T \sim \rho c r^2/3\kappa_\infty$, where r, ρ, and c are the radius, density, and specific heat of the particle, respectively, and κ_∞ is the thermal conductivity of the surrounding media.[45] For a 30 μm diameter particle ($r \sim 15$ μm) of CLC ($\rho \sim 950$ kg m^{-3}, $c \sim 1936$ J kg^{-1} K^{-1}) surrounded in water ($\kappa \sim 0.609$ W m^{-1} K^{-1}), this yields $\tau_T \sim 0.2$ ms. This time scale is much longer than the pulse length ($t_p \sim 5$ ns) of the excitation laser, so we may assume energy is effectively localized to the particle immediately after excitation. This initial spike in particle temperature, where $t_p < \tau_T$, is estimated by $\frac{\Delta T}{I_o} \approx \frac{3 t_p K_{abs}}{4 \rho c r}$, where ΔT is temperature change, I_o is the excitation intensity, and K_{abs} is the absorption conversion efficiency of the particle. From this relation, we see that the initial temperature change is independent of the surroundings and largely determined by the thermal properties of the LC compound and the fraction of laser power absorbed and then converted thermally. The particle then reaches equilibrium with the environment over the $\tau_T \sim 0.2$ ms time scale, well before the next subsequent pulse as determined by the laser repetition rate (<50 Hz, 20 ms pulse-to-pulse), and before the LC molecules can reorient due to changes in temperatures as determined by their time constant ($\tau_{LC} \sim >1$ ms). As a following pulse excites the particle, the emitted light effectively probes the thermally equilibrated state induced by the previous pulse. For thermal sensing applications, this allows undesired heat to dissipate throughout the environment and avoid significant localization. Figure 3a demonstrates this capability for a 50 μm microdroplet illuminated at 2 mJ cm^{-2} and repetition rates of 2−20 Hz. Across this range of repetition rates and powers, modest increases in temperature appear after 60 s of exposure (0.048 °C for 2 Hz, 0.072 °C for 5 Hz, 0.13 °C for 10 Hz, and 0.18 °C for 20 Hz). These results indicate that heating increases with increasing repetition rate and corresponding energy transfer to the microdoplets, but importantly can be minimized below 0.05 °C for low repetition rates. To quantify the temperature resolution of the entire measurement apparatus, the standard deviations of temperature are 0.015 °C, 0.0093 °C, 0.0087 °C, and 0.0093 °C for the 2 Hz, 5 Hz, 10 Hz, and 20 Hz data, respectively. The results have an average standard deviation and temperature resolution of ∼0.011 °C for this LC compound ($S \sim 4.1$ nm °C^{-1}, 47% COC, 26% CN, and 26% CC). The temperature resolution of droplets consisting of the more sensitive LC compound ($S \sim 300$ nm °C^{-1}, 30% COC, 60% CN, and 10% CD) requires further study with higher resolution environmental controls. Supplementary Figure S7 shows spectrograph images of lasing droplets from this highly sensitive compound after consecutive excitation pulses.

Alternatively, further increasing repetition rates and/or power can lead to controlled levels of heating, thereby suggesting a method for thermal modulation and remote control of local temperature. In this mode of operation, the droplets perform as functional photothermal probes, where active temperature feedback is possible through measurements of the wavelength of laser light emitted with each pulse. Figure

https://dx.doi.org/10.1021/acsnano.0c10234
ACS Nano 2021, 15, 2327−2339

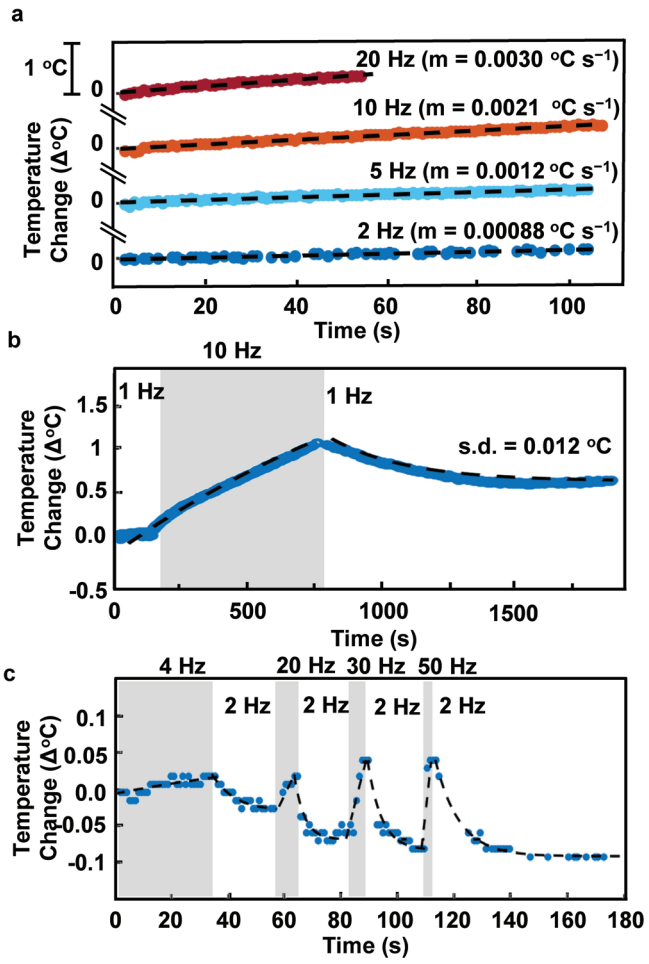

Figure 3. Laser-induced heating and additional modalities. (a) Temperature tracking of a 50 μm microdroplet laser as a function of excitation repetition rate and excited at 2 mJ cm^{-2}. The LC compound is 47% COC, 26% CN, and 26% CC and measured at 21 °C. (b) Repetitive excitation can induce localized heating to biologically relevant levels, in excess of 1 °C, that can be useful for controlled photothermal therapies with active, collocated temperature feedback. (c) Thermal transients relate to material properties of surrounding tissues. Repetition rates can be rapidly changed to induce transients with minimal changes in temperature (<0.05 °C). Compound in (b,c) is 33% COC, 41% CN, and 25% CC and measured at 37 °C.

3b demonstrates this active feedback by tracking the microdroplet temperature during changes in repetition rate for extended periods of time (30 min). Modulated from 1 to 10 Hz and back to 1 Hz, the temperature of the microdroplet displays the characteristic exponential rise and decay of a thermally driven system subject to processes of thermal diffusion. The system can be driven to biologically relavant temperature variations on the order of 1 °C, which may be useful in neurological applications where modulation is desired without incurring tissue damage (±2 °C).[4] The standard deviation at equilibrium is 0.012 °C, which indicates that the local heating mode of operation has the same variance and temperature resolution as the sensing modality. Quantitative analysis can yield information on the thermal properties of the environment[46] with direct analogues to methods employed in electronic systems.[47] Figure 3c demonstrates this concept by applying rapid changes in repetition rate at low excitation powers (2 mJ cm^{-2}) and heating timespans variable from 30 to 5 s. Incorporating heating control through repetition rate allows the precise measurement of temperature transients while inducing local heating <0.05 °C.

Collectively, these results outline three operational modalities: (1) sensing of temperature within minimal laser-induced heating, (2) thermal modulation with active feedback and control, and (3) frequency-dependent transient measurements with minimal heating which may allow for measurement of the thermal properties of surrounding materials. Precise measurement and dosing of heat can be valuable in photothermal therapies wherein a well-controlled, elevated temperature can induce apoptosis or neuromodulation,[48] while measurement of thermal transport properties of surrounding tissues can distinguish between normal state and inflammatory responses, as examples.

Gelatin Shell Degradation Dynamics. In addition to the measurement and control of temperature, the functional lifetime of biodegradable photothermal probes must match that of the disease, procedure, and injection site. After this time period, the probes degrade into naturally occurring chemicals and are resorbed or excreted from the body. Encapsulation in protective shells is a common strategy to maintain the structural integrity of microparticles within challenging environments.[49,50] If left unprotected within biological media, the oily cholesterol derivatives can coalesce and laminate to internal surfaces, thereby losing their functionality as temperature-sensitive lasers. As such, the lifetime and degradation properties of the protective gelatin shell affects the functional lifetime of the particles. Accelerated enzymatic degradation tests over a range of shell parameters reveal the mechanisms by which the cross-linked gelatin degrades. Encapsulated particles for these studies use the fabrication methods detailed previously but cross-linked with varying percentages of glutaraldehyde (0–5 wt %). Rinsing and centrifuging with PBS four times and then diluting 100 μL of particle slurry with 400 μL of cleavage buffer (100 mM NaCl and 50 mM Tris base; pH 8) create the working solutions. A stock solution of porcine pancreatic elastase (PPE) (10 mg/mL in H_2O) mimics the native proteolysis of gelatin *in vivo*. Accelerated degradation involves incubation of 10 μL of enzyme stock solution with 50 μL of the working solution at 37 °C, resulting in an elastase concentration of 1.66 mg/mL. Bright-field transmission micrographs at 1 min intervals highlight the degradation process, as in Figure 4a for a representative distribution of core oil droplet sizes, from 60 μm, 40 μm, and 0 μm. Initially, the differences in refractive index with the surrounding buffer solution yield clearly defined outlines of the gelatin shells. As hydrolysis progresses through cleavage of the comprising glycine- and alanine-rich proteins, the density of the shell decreases, with corresponding reductions in the refractive index. As such, the definition/contrast of the shell also decreases, as in Figure 4a. Similar decreases occur in the intensity of fluorescence from 5-carboxytetramethylrhodamine (5-TAMRA)-doped gelatin imaged with confocal microscopy (Supplementary Figure S8). As the hydrogel network continues to break down, the network rapidly swells with water and disintegrates. The dotted lines in the right most micrographs in Figure 4a identify the border of the shell at this rapid transition. After the structural disintegration of the shell, the CLC microdroplet, which is less dense than water, floats out of the field of view.

The size distribution within a single batch of microdroplets facilitates studies of the effect of droplet size on shell

https://dx.doi.org/10.1021/acsnano.0c10234
ACS Nano 2021, 15, 2327–2339

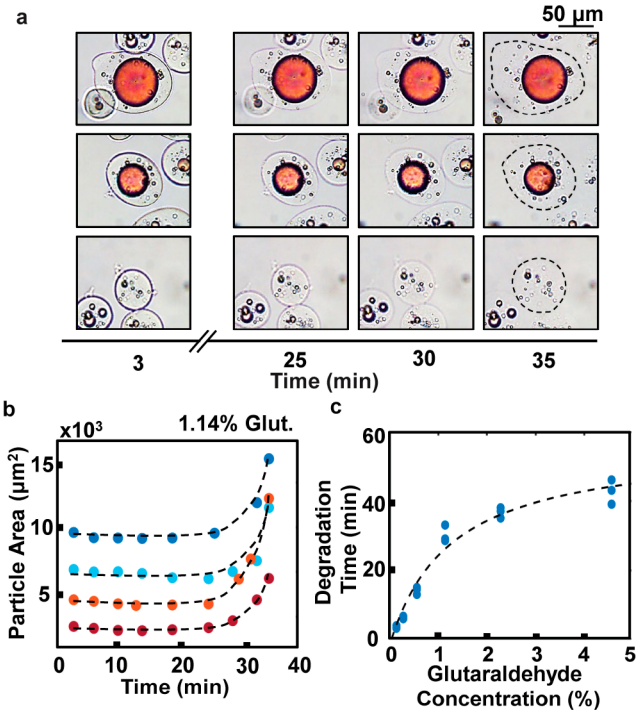

Figure 4. Accelerated enzymatic degradation and cross-linking dynamics. (a) Transmissive micrographs of encapsulated particles during enzymatic degradation at 37 °C. Each row paths the trajectory of particles of differing sizes and shell thicknesses. Particles are cross-linked in a 1.14% glutaraldehyde solution. (b) Particle area as a function of time obtained *via* image boundary analysis. Bulk degradation of the gelatin hydrogel shells results in a characteristic rapid disintegration and inflection point. (c) Tuning of bulk degradation time *via* percent of glutaraldehyde cross-linking agent.

degradation. Figure 4b shows a fixed area of individual particles (tracked through image processing algorithms implemented in Matlab) as a function of time for a representative sample cross-linked with glutaraldehyde at 1.14%. Interestingly, the area encompassed by the particles is largely invariant during proteolysis up until rapid disintegration, represented by the inflection point in the area of the particles. This disintegration time is largely independent of droplet size/shell size, consistent with a bulk, rather than a surface, mode of erosion. Furthermore, the time of disintegration does not depend on shell thickness (Supplementary Figure S9). Particles with the same total area and cross-linking percentage, but with different core−shell ratios display similar degradation profiles.

Figure 4c shows that the disintegration time depends strongly on the degree of glutaraldehyde-induced cross-linking between biopolymers within the gelatin matrix. This time asymptotically approaches a maximum (40−50 min) as a function of glutaraldehyde concentration used to initially synthesize the cross-linked matrix. The maximum cross-linking density likely depends on two main considerations: (1) the stoichiometric ratio of glutaraldehyde to active, primary amines from the gelatin starting material approach saturation, and/or (2) the continuously increased barrier to diffusion for glutaraldehyde as the gelatin solution exhibits more solid-like behavior through physical entanglement and reduced hydrophilicity.[51,52] The ability to tune the degradation time of the microparticle shell independent of optical function allows for tailoring of particles to specific injection sites, tissues, and/or disease states.

Comparisons of degradation times determined *in vitro* to those observed *in vivo* are complicated by large, biological variations in endogenous elastase concentrations, enzymatic activity, and disease state, along with other effects that can arise from mechanical/fluidic forces. For context, production of human neutrophil elastase (HNE) occurs in quantities up to 3 pg per cell.[53] At average cell diameters of 8.85 μm,[54] this production yields a maximum concentration of 8.26 mg/mL internal to the cell. Average concentrations of neutrophils within blood vary between 3−6 million per mL and 15−40 million per mL in individuals experiencing bacterial infection,[55] corresponding to an average concentration of 15 μg/mL and 37.5 μg/mL, respectively, upon release. Additionally, PPE can be 6 times more active than HNE in degrading human lung elastin.[56] As such, the effects highlighted in Figure 3 are, at PPE concentrations of 1.66 mg/mL, greatly accelerated, such that these results can serve as conservative lower limits on degradation times *in vivo*.

Once the hydrogel shells are removed, the remaining particle cores will undergo biodegradation. The LC compounds metabolize *via* cholesteryl esterase into cholesterol and the respective fatty acid of the compound, (*i.e.*, carbonic acid, benzoic acid, and nonanoic acid). Nile red is a commonly used organic fluorophore[57] and metabolizes *via* the cytochrome P450 3A4 (CYP3A4) enzyme into *N*-monoethyl and *N*-desethyl products.[58] This enzyme predominately resides in the liver and intestinal tract and oxidizes small foreign, organic molecules.

Cell Compatibility. A series of cell culture and proliferation tests yield initial assessments of the biocompatibility of the CLC microdroplet system. Encapsulated CLC microdroplets are introduced to cultures of mouse L929 fibroblast cells incubated in plate wells for 24 h and sink to the cell interfaces. Over the following 3 days, the cells grow up and around the gelatin shells. Figure 5a shows three-dimensional laser scanning confocal microscope data and image cross sections of a representative particle surrounded by cells. Dapi and f-actin fluorophores selectively stain the nuclei and intercellular regions blue and green, respectively, while the Nile Red within the CLC microdroplet identifies the oil core. Importantly, the particles function properly after 3 days of culturing with cells, as shown within the spectrographs of Figure 5b. Results of MTT assays (N = 3), highlighted in Figure 5c,d, define the degree of cell growth/inhibition for three particle concentrations and four glutaraldehyde percentages, prepared using procedures described previously. In addition to a control that does not involve particles, the results include a case for particles with uncross-linked shells, corresponding to 0% glutaraldehyde. Here the shells rapidly dissolve (<1 min) at the 37 °C incubation temperature, and the resulting CLC microdroplets float away. Nearly 100% cell proliferation compared to the control confirms that the chemical constituents of the shells are cytocompatible. Cell proliferation is largely unimpeded for the first two concentrations of particles, independent of initial cross-linker percentage. The highest concentration of particles, however, impedes proliferation on the second and third day of incubation. This result could be due to residual glutaraldehyde, given the increased volume of cross-linked gelatin shell, or due to the physical limitation of space imparted by the saturated layer of particles. Subsequent live/dead cell staining and

https://dx.doi.org/10.1021/acsnano.0c10234
ACS Nano 2021, 15, 2327−2339

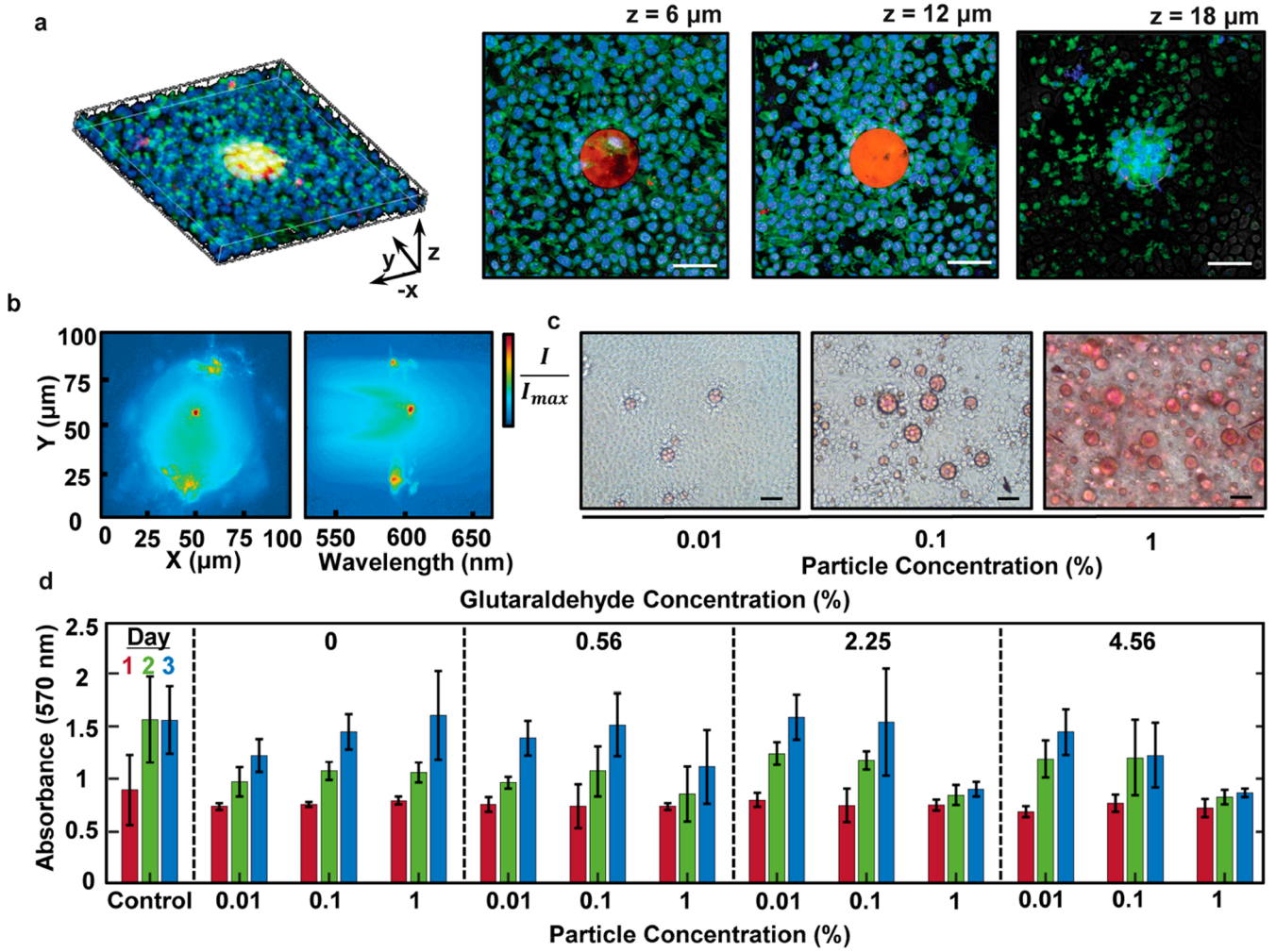

Figure 5. Cytotoxicity study of transient microdroplet lasers. (a) Scanning confocal micrographs depicting a 72 h culture of L929 cells surrounding a LC microdroplet laser. Dapi, f-actin, and nile red selectively label cell nuclei, intercellular regions, and the LC, respectively. Scale bars are 50 μm. (b) Imaging spectrographs of a particle after 72 h of incubation with cells showing the spatial and spectral signature of lasing. (c) Micrographs of L929 cells after 72 h of incubation for three variations of particle concentrations and four variations in cross-linker percentage. (d) Multiday results of cell compatibility testing *via* the MTT cell proliferation assay. The particles are not cytotoxic and only slightly inhibit cell growth at high particle concentrations and if cross-linked with high concentrations of glutaraldehyde. Sample size, N = 3. Error bars indicate maximum bounds of sample set.

fluorescence imaging (Supplementary Figure S10) indicate that the rate of cell death is not affected by any of the particle concentrations or cross-linker percentages. These combined results suggest that the encapsulated particles and their constituents are cytocompatible and are therefore appropriate for further exploration in *in vivo* models.

Lasing in Biological Tissue. The ability to deliver the microdroplets to targeted areas of tissues by syringe injection represents a key advantage over conventional implants for temperature sensing. Figure 6a shows a micrograph of a syringe during ejection of a microdroplet saturated solution into PBS, a mechanism for introducing thousands of independent, wireless temperature sensors. Casper fish, a species of zebrafish with genetic modifications that inhibit the production of melatonin to yield body tissues that are largely transparent to visible wavelengths, provides a vehicle to demonstrate the functionality of these systems in biological tissues. Figure 6b shows a picture of a Casper fish cadaver with a dotted box that depicts the area for subcutaneous particle injection. Imaging can occur directly through layers of tissue, as shown in Figure 6c, corresponding to the outermost surface of the scales, interstitial space, and muscle tissue. Figure 6d shows a reflectance micrograph of the outlined particle, captured with white light. Optical pumping yields emission highlighted by the corresponding spectrograph in Figure 6e, with peak emission from the center of the droplet, characteristic of Bragg lasing. The protective gelatin shell plays a critical role in preventing the CLC microdroplets from deforming or adhering to adjacent tissue surfaces and thereby losing their lasing functionality, as in Supplementary Figure S11.

The emission from the injected particle lasers is bright and observable by a camera (Google Pixel 3), suggesting the ability for imaging with inexpensive spectrometers. Figure 6f–i shows a series of pictures of a Casper fish cadaver in the focal spot of the microscope. Under incoherent white light illumination and in the absence of particles, the scattered light from the fish is white as expected, Figure 6f. With the same illumination conditions but with injected microdroplets, Figure 6g, the light emitted from the fish is red, indicative of the nile red dye. Figure 6h,i shows corresponding pictures under pulsed laser

https://dx.doi.org/10.1021/acsnano.0c10234
ACS Nano 2021, 15, 2327–2339

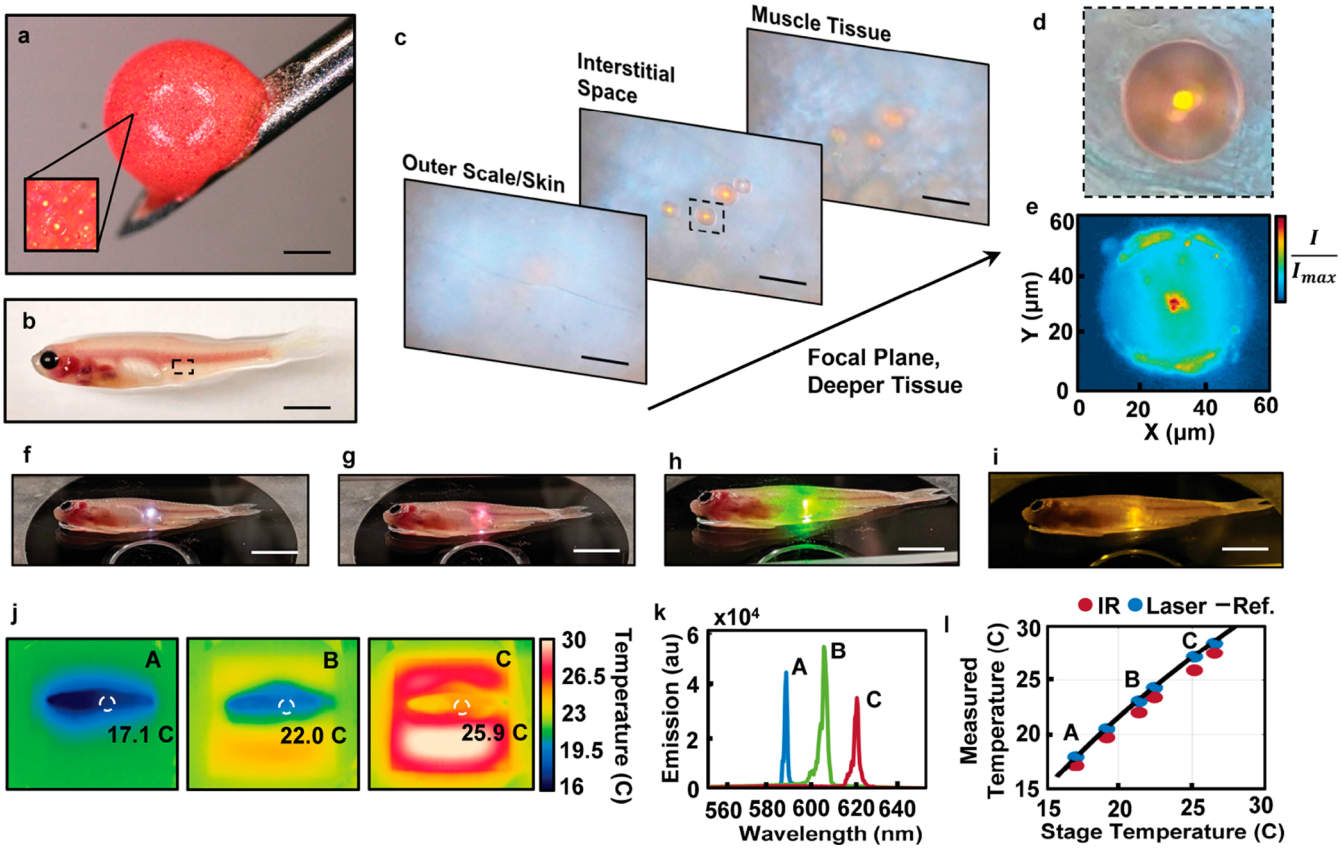

Figure 6. Lasing in *ex vivo* Casper fish. (a) Micrograph of a syringe needle ejecting a dispersion of encapsulated microdroplet lasers. Scale bar, 500 μm. (b) Camera image of *ex vivo* Casper fish and area outlined for injection. Scale bar, 5 mm. (c) Micrographs of injected particles at varying planes of tissue depth. While seemingly transparent, the tissue is translucent and semiscattering. Scale bar, 200 μm. (d) White-light micrograph of a single particle within the Casper fish and corresponding Bragg reflectance. (e) Imaging spectrograph depicting laser emission upon excitation with pulsed nanosecond nd:YAG laser. Unfiltered camera image of the Casper fish illuminated with white-light (f) without and (g) with particles. Laser excited particles within a Casper fish (h) without and (i) with 550 nm long pass filter. Scale bar, 5 mm. (j) Thermal thermography of the Casper fish at three different temperatures, 17.1 °C, 22.0 °C, and 25.9 °C, and labeled A, B, and C, respectively. (k) Laser emission from injected particles at the temperatures in (j). (l) Measured temperature obtained *via* the peak emission wavelength of the particles graphed with respect to temperature gained through thermal imaging (IR), stage thermocouple (stage), and the reference calibration of the LC compound (ref).

exposure. Accepting all outgoing light, the image in Figure 6h is dominated by the green excitation source. However, if the excitation wavelength is filtered out (Figure 6i), observable lightthat emanates from the fish tissue has a color/wavelength dependent on the local temperature. Varying the temperature of the Casper fish cadaver *via* a transparent heating stage allows measurements of the internal temperature as determined by the microdroplet emission wavelength.

To compare the temperature obtained from multiple technologies, Figure 6j shows infrared thermal images collected at three stage temperatures (17.86 °C, 23.11 °C, 27.27 °C with respect to an on-plate thermocouple), with temperatures of 17.1 °C, 22.0 °C, and 25.9 °C near the region of microdroplet injection. The emission wavelengths of the internal droplets are, in Figure 6k, mapped to temperature based on the CLC compound and compared to a reference thermocouple on the heating stage and that obtained from the thermal images in Figure 6l. The temperatures predicted from the lasing wavelengths (17.90 °C, 23.04 °C, 27.15 °C) are in close correspondence with those of the stage thermocouple (±0.1 °C), while the infrared measured values are uniformly cooler by ∼1 °C. These differences indicate the near-surface nature of the infrared measurement and the expected gradients in temperature through the thickness of the fish. This effect emphasizes the variation between internal and surface temperature measurements and the opportunity advanced optical probes have for accurate representations of internal temperatures.

CONCLUSIONS

This study establishes an important baseline of capabilities in materials science and optical engineering for biodegradable CLC lasers as biological temperature sensors and photothermal probes. Biologically derived cholestryl esters, organic fluorphores, and gletain/gum acacia copolymers form microcavity laser resonators through bulk and chemical self-assembly. When pumped optically, the bright and narrow emission of the microdroplets is advantageous compared to conventional molecular fluorophores, while the high sensitivity of the CLC resonator imparts a temperature sensitivity beyond that of alternative micro/nanolasers. The probes can be utilized in three different modalities: (1) temperature sensing, where self-heating is minimal, (2) thermal modulation, where temperature sensing accompanies laser-induced heating to establish a closed-feedback loop for active control, and (3) rapid and minute modulation of probe temperature, where

https://dx.doi.org/10.1021/acsnano.0c10234
ACS Nano 2021, 15, 2327−2339

analysis of decay profiles yields thermal transport properties of the surrounding media. Encapsulation *via* complex coacervation protects the particles within a hydrogel shell with independent control of thickness and degradation rates. In this manner, the probes can be tailored to a range of applications that require different functional lifetimes, such as short-term photothermal therapy sessions (days) *versus* long-term inflamation/implant monitoring (years). Additionally, cytotoxicity studies suggest limited effects on mouse L929 fibroblast cells and promise for *in vivo* testing.

These results represent the starting point for future efforts that will expand functionality to NIR operation and incorporate additional features, such as shell functionalization for triggered dissolution, simultaneous drug delivery, and targeting capabilities. For use in deep tissue regions, the operating wavelengths must lie within biological imaging windows (NIR I and II). The CLC material[59] and the schemes for forming, purifying, and encapsulating the droplets are broadly applicable. Development of LC-compatible fluorophores capable of excitation and emission in the NIR I and II regions remains a topic of current work. Attractive possibilities include up-conversion nanoparticles, quantum dots, or, alternatively, use of two-photon excitation schemes.

METHODS

Fabrication of Encapsulated Liquid Crystal Droplets. All chemicals were purchased from Sigma-Aldrich and used as received. A LC mixture consisting of 47 wt % cholesteryl oleyl carbonate (COC), 26 wt % cholesteryl nonanoate (CN), and 26 wt % cholesteryl chloride (CC) was magnetically stirred/vortexed at 70 °C until homogeneous. Nile red was added to the LC compound at 1 wt % and continually stirred at 70 °C until uniformly dispersed. To create the initial emulsion, 3 mL of a 10 wt % gelatin (porcine skin) was combined with 1.5 mL of the dye-doped LC compound within a 20 mL scintillator vial at 50 °C. The mixture was magnetically stirred at 1000 rpm for periods longer than 2 h to create an emulsion with the desired LC droplet size distribution. Under continued agitation, 3 mL of 10 wt % gum acacia solution (from acacia tree) was added. The pH of the emulsion was adjusted above 5 with a sodium hydroxide solution, and 8.3 mL volume of DI water was then gradually added. To induce conservation and formation of the hydrogel shell, the emulsion pH was adiabatically adjusted to 4.4 through dropwise addition of an acetic acid solution. Shell thickness can be controlled through the pH. The uniformity of the thickness depends largely on the conditions for agitation and speed of adjustment of the pH. At this point, samples can be taken, imaged in a microscope for desired shell properties, and the batch adjusted accordingly. If the shell is too large or nonuniform, the pH can be reset above the isoelectric point of the polymers to dissolve the hydrogel and tried again. A 25 wt % glutaraldehyde solution was then dropwise introduced to a final concentration of 0−5 wt % with respect to the total gelatin in solution. Under consistent agitation but lowered to 250 rpm, the emulsion was then rapidly cooled to 4 °C. After 1 h, the pH of the emulsion was adjusted to 9 with the addition of a sodium hydroxide solution to further solidify the shells. Without agitation, particles sink or float depending on the size ratio of LC core and gelatin shell. Selectively removing the floating particles and the remaining clear liquid phase created a dense slurry of encapsulated microparticles. The slurry can then be stored (in a dark place at slightly above freezing or room temperature), rinsed of cross-linker, or filtered based on size.

Optical Imaging and Characterization. Reflective micrograph images of Figure 1 were obtained with a digital microscope (VHX-5000, Keyence) under crossed polarization. The transmissive and unpolarized micrograph images in Figure 3 were obtained with an Olympus CHBS. The lasing experiments throughout were performed with a Q-switched, DPSS nd:YAG laser (SPOT 1-500-1064, Elforlight) emitting 1 ns pulses at 1064 nm which is frequency doubled with a heated KTP crystal to 532 nm. Repetition rate was controlled *via* an external signal generator and output power *via* an optical density filter wheel. This laser was focused into an inverted microscope (Eclipse Ti−U, Nikon), through a 20×/0.45 NA objective (S Plan Fluor, Nikon) to a 65 μm focal spot. Spot size was controlled through a translatable lens assembly before the microscope. Sample temperature was controlled with a heated indium tin oxide (ITO)-coated stage and controller (TC-1 Controller, Biosciences Tools). Power at the focal point was measured with a pyrometer (PM10 PowerMax, Coherent). Light emitted from the sample is separated from the 532 nm excitation laser *via* a long pass filter and imaged with spectrograph (Acton SP2300, Princeton Instruments).

Cell Culture. A mouse L929 cell line was cultured with the particles to evaluate the biocompatibility. Minimum essential medium Eagle (EMEM, Lonza) with 10% fetal bovine serum (FBS, Gibco) and 1% penicillin-streptomycin (PS, Invitrogen) was used as the cell culture medium.

MTT Assay. For the 96-well plate, 5×10^3 cells were seeded into each well, and the particles were added into the well after 2 days culture. Cell proliferation was quantified by The CyQUANT MTT Cell Viability Assay (MTT, Invitrogen, USA) at 24 h, 48 h, and 72 h after addition of particles. The cells were washed by replacing 100 μL of medium with fresh cell culture medium, to which 10 μL of the MTT stock solution is added. The plate is then incubated for 4 h at 37 °C. 100 μL of the SDS-HCl solution is then added to each well and incubated for another 4 h at 37 °C. Each sample is mixed, and the solution is extracted to read within a plate reader. The absorbance at 570 nm is measured by a Cytation 5 imaging reader (BioTek, USA). For each data point within the assay of Figure 5, there are three wells cultured with identical parameters, giving a sample size, $N = 3$.

Live/Dead Stain. The live/dead stain was performed in accordance to the manufacturer's instructions to image cellular viability. For the 96-well plate, 5×10^3 cells were seeded into each well, and the particles were added after 2 days of incubation. After 2 days, the samples were stained with a solution of calcein acetoxymethyl ester and propidium iodide (Invitrogen, USA) and mixed for 30 min in a dark room. The samples were washed with PBS and subsequently visualized using an inverted fluorescence microscope (Nikon, Japan). Images of representative microscopic fields were captured.

Cells F-Actin Fluorescent Stain. Cells were cultured for 3 days with particles and fixed with 4% formaldehyde for 30 min at room temperature. The samples were then washed three times with PBS to remove the fixing solution. Incubation with 0.1% Triton-X-100 for 5 min at room temperature permeabilized the cell membrane. Then, after washing three times with PBS, the samples were blocked with 1% BSA in PBS at room temperature for 1 h. After removing the blocking reagent, the samples were stained with F-actin marker rhodamine-phalloidin (Invitrogen, USA) at room temperature for 40 min and then counterstained with 4′,6-diamidino-2-phenylindole (Invitrogen, USA) for 10 min. Images were obtained through Leica SP8 confocal microscope (Leica, Germany)

ASSOCIATED CONTENT

Supporting Information

The Supporting Information is available free of charge at https://pubs.acs.org/doi/10.1021/acsnano.0c10234.

Cholesteric liquid crystal composition and temperature dynamics (Figure S1); variable shell thickness *via* coacervation pH (Figure S2); robustness of LC orientation to particle deformation (Figure S3); characterization of pump laser (Figure S4); Nile Red concentration and particle lasing (Figure S5); line widths and resonance efficiencies of lasing particles (Figure S6); lasing in highly sensitive LC droplet (Figure S7); scanning confocal microscopy of gelatin

https://dx.doi.org/10.1021/acsnano.0c10234
ACS Nano 2021, 15, 2327−2339

degradation (Figure S8); accelerated enzymatic degradation *vs* shell thickness (Figure S9); live/dead cell staining (Figure S10); and unencapsulated particles in Casper fish model (Figure S11) (PDF)

AUTHOR INFORMATION

Corresponding Author

John A. Rogers − *Department of Materials Science and Engineering, Querrey-Simpson Institute for Bioelectronics, Department of Chemistry, Department of Biomedical Engineering, Department of Mechanical Engineering, Department of Neurological Surgery, and Department of Electrical and Computer Engineering, Northwestern University, Evanston, Illinois 60208, United States;* orcid.org/0000-0002-2980-3961; Email: jrogers@northwestern.edu

Authors

Daniel Franklin − *Department of Materials Science and Engineering and Querrey-Simpson Institute for Bioelectronics, Northwestern University, Evanston, Illinois 60208, United States;* orcid.org/0000-0002-6453-5114

Tyler Ueltschi − *Department of Chemistry, Northwestern University, Evanston, Illinois 60208, United States*

Andrea Carlini − *Querrey-Simpson Institute for Bioelectronics, Northwestern University, Evanston, Illinois 60208, United States*

Shenglian Yao − *Querrey-Simpson Institute for Bioelectronics, Northwestern University, Evanston, Illinois 60208, United States*

Jonathan Reeder − *Department of Materials Science and Engineering and Querrey-Simpson Institute for Bioelectronics, Northwestern University, Evanston, Illinois 60208, United States;* orcid.org/0000-0002-7624-7355

Benjamin Richards − *Department of Materials Science and Engineering, Northwestern University, Evanston, Illinois 60208, United States*

Richard P. Van Duyne − *Department of Chemistry, Northwestern University, Evanston, Illinois 60208, United States;* orcid.org/0000-0001-8861-2228

Complete contact information is available at: https://pubs.acs.org/10.1021/acsnano.0c10234

Author Contributions

D.F. and J.R developed the concept. D.F., T.U., A.C., S.Y., J.R., and B.R. performed experiments. D.F. analyzed data. D.F. and J.R wrote the manuscript and all authors edited.

Notes

The authors declare no competing financial interest.

ACKNOWLEDGMENTS

Co-author Richard P. Van Duyne passed away July 28, 2019. We acknowledge support from the Querrey Simpson Institute for Bioelectronics at Northwestern University. Microscopy was performed at the Biological Imaging Facility at Northwestern University (RRID:SCR_017767), graciously supported by the Chemistry for Life Processes Institute, the NU Office for Research, the Department of Molecular Biosciences, and the Rice Foundation. We would like to thank H. Zhang for the use of his Q-switched, DPSS nd:YAG laser. We would also like to thank S. Lazzara of LCR Hallcrest for the very interesting and fruitful conversations.

REFERENCES

(1) Rosenfeld, D.; Senko, A. W.; Moon, J.; Yick, I.; Varnavides, G.; Gregurec, D.; Koehler, F.; Chiang, P. H.; Christiansen, M. G.; Maeng, L. Y.; Widge, A. S.; Anikeeva, P. Transgene-Free Remote Magnetothermal Regulation of Adrenal Hormones. *Sci. Adv.* **2020**, *6* (15), eaaz3734.

(2) Rastinehad, A. R.; Anastos, H.; Wajswol, E.; Winoker, J. S.; Sfakianos, J. P.; Doppalapudi, S. K.; Carrick, M. R.; Knauer, C. J.; Taouli, B.; Lewis, S. C.; Tewari, A. K.; Schwartz, J. A.; Canfield, S. E.; George, A. K.; West, J. L.; Halas, N. J. Gold Nanoshell-Localized Photothermal Ablation of Prostate Tumors in a Clinical Pilot Device Study. *Proc. Natl. Acad. Sci. U. S. A.* **2019**, *116* (37), 18590−18596.

(3) Nam, J.; Son, S.; Park, K. S.; Zou, W. P.; Shea, L. D.; Moon, J. J. Cancer Nanomedicine for Combination Cancer Immunotherapy. *Nat. Rev. Mater.* **2019**, *4* (6), 398−414.

(4) Owen, S. F.; Liu, M. H.; Kreitzer, A. C. Thermal Constraints on *in Vivo* Optogenetic Manipulations. *Nat. Neurosci.* **2019**, *22* (7), 1061−1065.

(5) Guatteo, E.; Chung, K. K.; Bowala, T. K.; Bernardi, G.; Mercuri, N. B.; Lipski, J. Temperature Sensitivity of Dopaminergic Neurons of the Substantia Nigra Pars Compacta: Involvement of Transient Receptor Potential Channels. *J. Neurophysiol.* **2005**, *94* (5), 3069−80.

(6) Chen, R.; Romero, G.; Christiansen, M. G.; Mohr, A.; Anikeeva, P. Wireless Magnetothermal Deep Brain Stimulation. *Science* **2015**, *347* (6229), 1477−80.

(7) Seo, D.; Neely, R. M.; Shen, K.; Singhal, U.; Alon, E.; Rabaey, J. M.; Carmena, J. M.; Maharbiz, M. M. Wireless Recording in the Peripheral Nervous System with Ultrasonic Neural Dust. *Neuron* **2016**, *91* (3), 529−39.

(8) Gutruf, P.; Krishnamurthi, V.; Vazquez-Guardado, A.; Xie, Z. Q.; Banks, A.; Su, C. J.; Xu, Y. S.; Haney, C. R.; Waters, E. A.; Kandela, I.; Krishnan, S. R.; Ray, T.; Leshock, J. P.; Huang, Y. G.; Chanda, D.; Rogers, J. A. Fully Implantable Optoelectronic Systems for Battery-Free, Multimodal Operation in Neuroscience Research. *Nat. Electron.* **2018**, *1* (12), 652−660.

(9) Martino, N.; Kwok, S. J. J.; Liapis, A. C.; Forward, S.; Jang, H.; Kim, H. M.; Wu, S. J.; Wu, J.; Dannenberg, P. H.; Jang, S. J.; Lee, Y. H.; Yun, S. H. Wavelength-Encoded Laser Particles for Massively Multiplexed Cell Tagging. *Nat. Photonics* **2019**, *13* (10), 720−727.

(10) Fikouras, A. H.; Schubert, M.; Karl, M.; Kumar, J. D.; Powis, S. J.; Di Falco, A.; Gather, M. C. Non-Obstructive Intracellular Nanolasers. *Nat. Commun.* **2018**, *9* (1), 4817.

(11) Koo, J.; MacEwan, M. R.; Kang, S. K.; Won, S. M.; Stephen, M.; Gamble, P.; Xie, Z.; Yan, Y.; Chen, Y. Y.; Shin, J.; Birenbaum, N.; Chung, S.; Kim, S. B.; Khalifeh, J.; Harburg, D. V.; Bean, K.; Paskett, M.; Kim, J.; Zohny, Z. S.; Lee, S. M.; Zhang, R.; Luo, K.; Ji, B.; Banks, A.; Lee, H. M.; Huang, Y.; Ray, W. Z.; Rogers, J. A. Wireless Bioresorbable Electronic System Enables Sustained Nonpharmacological Neuroregenerative Therapy. *Nat. Med.* **2018**, *24* (12), 1830−1836.

(12) Wang, X. D.; Wolfbeis, O. S.; Meier, R. J. Luminescent Probes and Sensors for Temperature. *Chem. Soc. Rev.* **2013**, *42* (19), 7834−69.

(13) Hong, G.; Diao, S.; Chang, J.; Antaris, A. L.; Chen, C.; Zhang, B.; Zhao, S.; Atochin, D. N.; Huang, P. L.; Andreasson, K. I.; Kuo, C. J.; Dai, H. Through-Skull Fluorescence Imaging of the Brain in a New Near-Infrared Window. *Nat. Photonics* **2014**, *8* (9), 723−730.

(14) Fernandez-Bravo, A.; Yao, K.; Barnard, E. S.; Borys, N. J.; Levy, E. S.; Tian, B.; Tajon, C. A.; Moretti, L.; Altoe, M. V.; Aloni, S.; Beketayev, K.; Scotognella, F.; Cohen, B. E.; Chan, E. M.; Schuck, P. J. Continuous-Wave Upconverting Nanoparticle Microlasers. *Nat. Nanotechnol.* **2018**, *13* (7), 572−577.

(15) Gu, Y.; Guo, Z.; Yuan, W.; et al. High-Sensitivity Imaging of Time-Domain Near Infrared Light Transducer. *Nat. Photonics* **2019**, *13*, 525−531.

(16) del Rosal, B.; Ruiz, D.; Chaves-Coira, I.; Juarez, B. H.; Monge, L.; Hong, G. S.; Fernandez, N.; Jaque, D. *In Vivo* Contactless Brain Nanothermometry. *Adv. Funct. Mater.* **2018**, *28* (52), 1806088.

(17) Schubert, M.; Woolfson, L.; Barnard, I. R. M.; Dorward, A. M.; Casement, B.; Morton, A.; Robertson, G. B.; Appleton, P. L.; Miles, G. B.; Tucker, C. S.; Pitt, S. J.; Gather, M. C. Monitoring Contractility in Cardiac Tissue with Cellular Resolution Using Biointegrated Microlasers. *Nat. Photonics* **2020**, *14* (7), 452−458.
(18) Qiao, B.; Luo, Y.; Cheng, H. B.; Ren, J.; Cao, J.; Yang, C.; Liang, B.; Yang, A.; Yuan, X.; Li, J.; Deng, L.; Li, P.; Ran, H. T.; Hao, L.; Zhou, Z.; Li, M.; Zhang, Y.; Timashev, P. S.; Liang, X. J.; Wang, Z. Artificial Nanotargeted Cells with Stable Photothermal Performance for Multimodal Imaging-Guided Tumor-Specific Therapy. *ACS Nano* **2020**, *14* (10), 12652−12667.
(19) Lee, W.; Jeon, M.; Choi, J.; Oh, C.; Kim, G.; Jung, S.; Kim, C.; Ye, S.-J.; Im, H.-J. Europium-Diethylenetriaminepentaacetic Acid Loaded Radioluminescence Liposome Nanoplatform for Effective Radioisotope-Mediated Photodynamic Therapy. *ACS Nano* **2020**, *14*, 13004−13015.
(20) Xu, M.; Zou, X.; Su, Q.; Yuan, W.; Cao, C.; Wang, Q.; Zhu, X.; Feng, W.; Li, F. Ratiometric Nanothermometer *in Vivo* Based on Triplet Sensitized Upconversion. *Nat. Commun.* **2018**, *9* (1), 2698.
(21) Sekiyama, S.; Umezawa, M.; Kuraoka, S.; Ube, T.; Kamimura, M.; Soga, K. Temperature Sensing of Deep Abdominal Region in Mice by Using Over-1000 nm Near-Infrared Luminescence of Rare-Earth-Doped NaYF4 Nanothermometer. *Sci. Rep.* **2018**, *8*, 16979.
(22) Brites, C. D. S.; Balabhadra, S.; Carlos, L. D. Lanthanide-Based Thermometers: At the Cutting-Edge of Luminescence Thermometry. *Adv. Opt. Mater.* **2019**, *7* (5), 1801239.
(23) Okabe, K.; Inada, N.; Gota, C.; Harada, Y.; Funatsu, T.; Uchiyama, S. Intracellular Temperature Mapping with a Fluorescent Polymeric Thermometer and Fluorescence Lifetime Imaging Microscopy. *Nat. Commun.* **2012**, *3*, 705.
(24) Shen, Y. L.; Lifante, J.; Fernandez, N.; Jaque, D.; Ximendes, E. *In Vivo* Spectral Distortions of Infrared Luminescent Nanothermometers Compromise Their Reliability. *ACS Nano* **2020**, *14* (4), 4122−4133.
(25) Chen, Y. C.; Fan, X. D. Biological Lasers for Biomedical Applications. *Adv. Opt. Mater.* **2019**, *7* (17), 1900377.
(26) Humar, M.; Yun, S. H. Intracellular Microlasers. *Nat. Photonics* **2015**, *9* (9), 572−576.
(27) Humar, M.; Dobravec, A.; Zhao, X.; Yun, S. H. Biomaterial Microlasers Implantable in the Cornea, Skin, and Blood. *Optica* **2017**, *4* (9), 1080−1085.
(28) Li, Y.; Jun-Yan Suen, J.; Prince, E.; Larin, E. M.; Klinkova, A.; Therien-Aubin, H.; Zhu, S.; Yang, B.; Helmy, A. S.; Lavrentovich, O. D.; Kumacheva, E. Colloidal Cholesteric Liquid Crystal in Spherical Confinement. *Nat. Commun.* **2016**, *7*, 12520.
(29) Lee, S. S.; Kim, J. B.; Kim, Y. H.; Kim, S. H. Wavelength-Tunable And Shape-Reconfigurable Photonic Capsule Resonators Containing Cholesteric Liquid Crystals. *Sci. Adv.* **2018**, *4* (6), eaat8276.
(30) Dudok, T. H.; Nastishin, Y. A. Optically Pumped Mirrorless Lasing. A Review. Part II. Lasing in Photonic Crystals and Microcavities. *Ukr. J. Phys. Opt.* **2014**, *15* (2), 47−67.
(31) Humar, M.; Musevic, I. 3D Microlasers from Self-Assembled Cholesteric Liquid-Crystal Microdroplets. *Opt. Express* **2010**, *18* (26), 26995−7003.
(32) van der Werff, L. C.; Robinson, A. J.; Kyratzis, I. L. Combinatorial Approach for the Rapid Determination of Thermochromic Behavior of Binary and Ternary Cholesteric Liquid Crystalline Mixtures. *ACS Comb. Sci.* **2012**, *14* (11), 605−12.
(33) Green, B.; Schleicher, L. Oil-Containing Microscopic Capsules and Method of Making Them. Patent US2800457A, July, 23, 1957.
(34) Piacentini, E.; Giorno, L.; Dragosavac, M. M.; Vladisavljevic, G. T.; Holdich, R. G. Microencapsulation of Oil Droplets Using Cold Water Fish Gelatine/Gum Arabic Complex Coacervation by Membrane Emulsification. *Food Res. Int.* **2013**, *53* (1), 362−372.
(35) *Handbook of Thermochromic Liquid Crystal Technology*; LCRHallcrest: Glenview, IL, 2014. https://www.hallcrest.com/support-documentation/entryid/744 (accessed 2020-12-30).
(36) Bigi, A.; Cojazzi, G.; Panzavolta, S.; Rubini, K.; Roveri, N. Mechanical and Thermal Properties of Gelatin Films at Different Degrees of Glutaraldehyde Crosslinking. *Biomaterials* **2001**, *22*, 763−768.
(37) Popov, N.; Honaker, L. W.; Popova, M.; Usol'tseva, N.; Mann, E. K.; Jakli, A.; Popov, P. Thermotropic Liquid Crystal-Assisted Chemical and Biological Sensors. *Materials* **2018**, *11* (1), 20.
(38) Krishna, M. M. G. Excited-State Kinetics of the Hydrophobic Probe Nile Red in Membranes and Micelles. *J. Phys. Chem. A* **1999**, *103* (19), 3589−3595.
(39) Martinez, V.; Henary, M. Nile Red and Nile Blue: Applications and Syntheses of Structural Analogues. *Chem. - Eur. J.* **2016**, *22* (39), 13764−13782.
(40) Cao, W.; Palffy-Muhoray, P.; Taheri, B.; Marino, A.; Abbate, G. Lasing Thresholds of Cholesteric Liquid Crystals Lasers. *Mol. Cryst. Liq. Cryst.* **2005**, *429* (1), 101.
(41) Mavrogordatos, T. K.; Morris, S. M.; Castles, F.; Hands, P. J.; Ford, A. D.; Coles, H. J.; Wilkinson, T. D. Density of Photon States in Dye-Doped Chiral Nematic Liquid Crystal Cells in the Presence of Losses and Gain. *Phys. Rev. E* **2012**, *86*, 011705.
(42) Sanz-Enguita, G.; Ortega, J.; Folcia, C. L.; Aramburu, I.; Etxebarria, J. Role of the Sample Thickness on the Performance of Cholesteric Liquid Crystal Lasers: Experimental, Numerical, and Analytical Results. *J. Appl. Phys.* **2016**, *119* (7), 073102.
(43) Zhao, L. Y.; Wang, Y.; Yuan, Y. G.; Liu, Y. J.; Liu, S. Q.; Sun, W. M.; Yang, J.; Li, H. Y. Whispering Gallery Mode Laser Based on Cholesteric Liquid Crystal Microdroplets as Temperature Sensor. *Opt. Commun.* **2017**, *402*, 181−185.
(44) Huang, Y. H.; Zhou, Y.; Wu, S. T. Lasing in Dye-Doped Photonic Liquid Crystal Devices. *Mol. Cryst. Liq. Cryst.* **2006**, *453*, 251−262.
(45) Pustovalov, V; Astafyeva, L; Jean, B Computer Modeling of the Optical Properties and Heating of Spherical Gold and Silica-Gold Nanoparticles for Laser Combined Imaging and Photothermal Treatment. *Nanotechnology* **2009**, *20* (22), 225105.
(46) Heber, A.; Selmke, M.; Cichos, F. Thermal Diffusivity Measured Using a Single Plasmonic Nanoparticle. *Phys. Chem. Chem. Phys.* **2015**, *17* (32), 20868−72.
(47) Cahill, D. G. Thermal Conductivity Measurement from 30 to 750 K: The 3ω Method. *Rev. Sci. Instrum.* **1990**, *61* (2), 802−808.
(48) Won, S. M.; Song, E.; Reeder, J. T.; Rogers, J. A. Emerging Modalities and Implantable Technologies for Neuromodulation. *Cell* **2020**, *181* (1), 115−135.
(49) Lee, S. S.; Kim, B.; Kim, S. K.; Won, J. C.; Kim, Y. H.; Kim, S. H. Robust Microfluidic Encapsulation of Cholesteric Liquid Crystals toward Photonic Ink Capsules. *Adv. Mater.* **2015**, *27* (4), 627−33.
(50) Lee, S. S.; Seo, H. J.; Kim, Y. H.; Kim, S. H. Structural Color Palettes of Core-Shell Photonic Ink Capsules Containing Cholesteric Liquid Crystals. *Adv. Mater.* **2017**, *29* (23), 1606894.
(51) Zustiak, S. P.; Boukari, H.; Leach, J. B. Solute Diffusion and Interactions in Cross-Linked Poly(Ethylene Glycol) Hydrogels Studied by Fluorescence Correlation Spectroscopy. *Soft Matter* **2010**, *6* (15), 3609.
(52) Wu, Y.; Joseph, S.; Aluru, N. R. Effect of Cross-Linking on the Diffusion of Water, Ions, and Small Molecules in Hydrogels. *J. Phys. Chem. B* **2009**, *113* (11), 3512−20.
(53) Janoff, A. Elastase in Tissue Injury. *Annu. Rev. Med.* **1985**, *36* (36), 207−16.
(54) Niemiec, M. J.; De Samber, B.; Garrevoet, J.; Vergucht, E.; Vekemans, B.; De Rycke, R.; Bjorn, E.; Sandblad, L.; Wellenreuther, G.; Falkenberg, G.; Cloetens, P.; Vincze, L.; Urban, C. F. Trace Element Landscape of Resting and Activated Human Neutrophils on the Sub-Micrometer Level. *Metallomics* **2015**, *7* (6), 996−1010.
(55) Li, Y. M.; Karlin, A.; Loike, J. D.; Silverstein, S. C. A Critical Concentration of Neutrophils is Required for Effective Bacterial Killing in Suspension. *Proc. Natl. Acad. Sci. U. S. A.* **2002**, *99* (12), 8289−8294.

https://dx.doi.org/10.1021/acsnano.0c10234
ACS Nano 2021, 15, 2327−2339

(56) Reilly, C. F.; Travis, J. The Degradation of Human Lung Elastin by Neutrophil Proteinases. *Biochim. Biophys. Acta, Protein Struct.* **1980**, *621* (1), 147−57.
(57) Li, W.; Terry, R. N.; Tang, J.; Feng, M. R.; Schwendeman, S. P.; Prausnitz, M. R. Rapidly Separable Microneedle Patch for the Sustained Release of a Contraceptive. *Nat. Biomed. Eng.* **2019**, *3* (3), 220−229.
(58) Lampe, J. N.; Fernandez, C.; Nath, A.; Atkins, W. M. Nile Red Is a Fluorescent Allosteric Substrate of Cytochrome P450 3A4. *Biochemistry* **2008**, *47* (2), 509−516.
(59) Hands, P. J. W.; Dobson, C. A.; Morris, S. M.; Qasim, M. M.; Gardiner, D. J.; Wilkinson, T. D.; Coles, H. J. Wavelength-Tuneable Liquid Crystal Lasers from the Visible to the Near-Infrared. *Proc. SPIE* **2011**, *8114*, 81140T.

https://dx.doi.org/10.1021/acsnano.0c10234
ACS Nano 2021, 15, 2327−2339